Frontiers of Information Technology & Electronic Engineering
www.jzus.zju.edu.cn; engineering.cae.cn; www.springerlink.com
ISSN 2095-9184 (print); ISSN 2095-9230 (online)
E-mail: jzus@zju.edu.cn

Performance enhancement for antipodal Vivaldi antenna modulated by a high-permittivity metasurface lens*

Shaopeng PAN[1], Mingtuan LIN[2], Lin QI[1], Pan CHEN[1], Yang FENG[1], Gaosheng LI†‡[1]

[1]*College of Electrical and Information Engineering, Hunan University, Changsha 410082, China*

[2]*College of Electronic Science, National University of Defense Technology, Changsha 410073, China*

†E-mail: Gaosheng7070@vip.163.com

Received Mar. 15, 2021; Revision accepted Apr. 28, 2021; Crosschecked Oct. 20, 2021

Abstract: A metasurface unit is designed operating at 2–20 GHz to enhance the gain and radiation performance of an antipodal Vivaldi antenna (AVA). The unit has a simple structure, stable ultra-wideband performance, high permittivity, and can independently modulate two polarization modes electromagnetic waves. We analyze the current distribution on the unit and extract equivalent characteristic parameters to verify the ability of independent modulation on two polarization modes electromagnetic waves. The designed metasurface unit is integrated into the aperture of the AVA and forms the metasurface lens (ML) for guiding the propagation of electromagnetic waves. Two types of ML are proposed and integrated into the AVA to design antennas Ant1 and Ant2. The modulation effect of the lens on the electromagnetic wave is analyzed from the perspective of electric field amplitude and phase, and the final design is obtained. From the optimized design results, the AVA and the proposed Ant2 are fabricated and measured, and the measurement results are in good agreement with the simulation ones. The impedance bandwidth measured by Ant2 basically covers the 2–18 GHz frequency band. Compared with the conventional AVA, the gain of the proposed Ant2 is increased by 0.6–3.7 dB, the sidelobe level is significantly reduced, and the directivity has also been clearly improved.

Key words: Antipodal Vivaldi antenna (AVA); Ultra-wideband; High-permittivity; Dual-polarization; Metasurface lens (ML)
https://doi.org/10.1631/FITEE.2100139 **CLC number:** TN82

1 Introduction

The massive popularity of wireless communication devices has made spectrum resources in increasingly short supply, and stimulated more demanding requirements for communication capacity and speed. The antenna is an indispensable device for wireless communication systems. To satisfy the high-capacity and high-speed transmission requirements of communication, an antenna is required to have stable ultra-wideband and high-gain performance. As a commonly used ultra-wideband antenna, the Vivaldi antenna (VA) has the advantages of wide bandwidth, low profile, simple structure, and easy fabrication (Lewis et al., 1974). Gibson (1979) proposed the planar structure of the VA, and this is widely used in many fields as a typical tapered slot antenna (Zhuge and Yarovoy, 2011; Martín-Neira et al., 2014; Yan et al., 2016). The conventional VA is composed mainly of the radiating plate and feeding structure with a coupled feeding method for excitation. It is easy for this kind of feeding method to cause energy leakage, and the impedance characteristic of the feeding structure is more sensitive to size, which brings inconvenience in practical applications. Gazit (1988) improved the feed structure of the VA, and the antipodal Vivaldi antenna (AVA) was designed. The radiating plates of the AVA were distributed on the upper and lower layers of the dielectric plate, so that the dual-parallel microstrip line could be used to feed the antenna. This simplified the feed structure. Zhao et al. (2017) proposed an improved tapered slot

‡ Corresponding author

* Project supported by the Open Fund for the Key Laboratory of Complex Systems Control and Intelligent Collaborative Technology, China (No. CSCIC191001)

ORCID: Shaopeng PAN, https://orcid.org/0000-0001-5589-365X; Gaosheng LI, https://orcid.org/0000-0001-5230-1428

antenna based on a post-wall structured slot line, which improved the cross-polarization levels and enlarged the bandwidth significantly.

In the low-frequency band, the operating mode of the AVA is the resonance mode, while it is in the traveling wave mode in the high-frequency band. When the phase difference of the current on the two radiators is 180°, the antenna has good end-fire radiation performance. However, as the frequency increases, the phase difference of the current on the two radiators is no longer stable, which will cause gain deterioration in the high-frequency band (Nassar and Weller, 2015). Therefore, the instability of directivity and gain of the AVA is a major challenge in application. Some techniques have been studied to enhance the gain and radiation performance of the antenna. Nassar and Weller (2015) introduced a parasitic elliptical metal patch at the aperture of the AVA to enhance the coupling between the two radiators. This enhanced the radiation gain and directivity of the antenna. In addition, some similar techniques, such as loading high dielectric constant plate (Bourqui et al., 2010), directors (Herzi et al., 2015), and dielectric lens (Moosazadeh and Kharkovsky, 2016) are used in the antenna aperture to enhance the gain. However, these methods make the structure of the antenna more complicated, and even lose the advantage of low profile. The development of metamaterial and metasurface and their application in the microwave field have brought new inspiration to antenna design. In Zhou and Cui (2011) and Zhou et al. (2011a), single- and multi-layer compact anisotropic zero-refractive index metamaterials were proposed. The metamaterials were integrated into the VA to improve the gain and directivity. Then, Zhou et al. (2011b) proposed a VA whose beam can be steered with a frequency based on the composite metamaterial Luneburg lens. As a two-dimensional structure, the metasurface has unique structural features that can achieve good control and modulation of electromagnetic waves. This can also be used to enhance the antenna radiation performance (Sun et al., 2013; Liu et al., 2020). In view of the limitations of traditional loading technology, loading methods based on metasurface technology have been studied to improve the AVA radiation performance. In Chen et al. (2015), the non-resonant parallel line unit was integrated into the aperture of the AVA. The unit has a single polarization modulation effect on electromagnetic waves. This increases the antenna gain in the 6–19 GHz frequency band. Zhu et al. (2018, 2019) integrated the metasurface structure into the AVA array and the double-slot VA, which realized a miniaturized design and improved the radiation gain of the antenna. While the metasurface unit used is relatively complicated, there are many optimization parameters. Guo et al. (2019) and Sang et al. (2020) designed two types of three-dimensional metasurface lenses (MLs) and integrated them on the aperture of the AVA to enhance the radiation gain. Compared with the traditional dielectric lens, the ML has the advantages of low profile and simple structure. However, the three-dimensional lens increases the profile and design complexity of the antenna. Yesilyurt and Turhan-Sayan (2020) designed a two-dimensional ML that operates in the 1–6 GHz frequency band. In the operating frequency band, the radiation gain and directivity are significantly enhanced, but the operating bandwidth of the ML limits the ultra-wideband performance of the AVA while the gain of the antenna with the ML at high frequency is deteriorated.

To enhance the radiation performance of the AVA, we design a metasurface unit which has a simple structure and is easy to implement. It can perform multi-octave bandwidth modulation of two polarization modes electromagnetic waves. We simulate and verify the independent modulation effect of the metasurface unit on the two polarization modes electromagnetic waves. Two types of ML are designed and integrated into the aperture of the AVA, and the guidance and modulation effects on the radiation field are analyzed from the perspective of the electric field. The final loading method and antenna form are determined through optimization of the structure. The ML significantly enhances the radiation gain and directivity of the AVA.

2 Conventional antenna design

Fig. 1 shows the designed AVA structure. The antenna slot is enclosed by exponential curves, which can be determined by Eqs. (1) and (2):

$$y_1 = \mathrm{e}^{\alpha_1 x} + c_1, \tag{1}$$

$$y_2 = e^{\alpha_2 x} + c_2, \quad (2)$$

where α_1 and α_2 are the curvature of the gradient lines, c_1 and c_2 are determined by the width of the antenna feed line. The substrate is Rogers 5880 with a dielectric constant of 2.2. The S_{11} simulation of the AVA is shown in Fig. 2a. It basically satisfies S_{11}<−10 dB in the 2–20 GHz frequency band, and only has a slight disturbance in the 3–3.5 GHz frequency band. Fig. 2b shows the simulated gain of the antenna with a maximum gain of 11.8 dB. The radiation gain of the original AVA is lower, which limits its application in some fields. Therefore, we propose a high-permittivity ML to enhance the radiation performance of the antenna.

3 Antenna with metasurface lens design

3.1 Unit design of the metasurface lens

As shown in Fig. 3, in our previous work (Pan et al., 2021), the designed metasurface lens unit (MLu) is composed of two rectangular metal arms L_1 and L_2 with a width of 0.3 mm. When the polarizion direction of the electromagnetic wave is along the x axis and y axis, the simulated S-parameters and surface current distribution are shown in Figs. 4 and 5, respectively. The frequency responses of the MLu to two polarization modes electromagnetic waves are basically the same. There is no resonance frequency in the 2–20 GHz frequency band, and S_{11}<−10 dB. This completely covers the operating frequency band

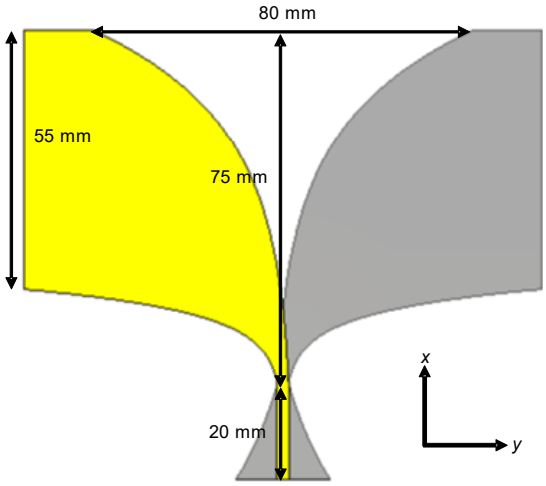

Fig. 1 Structure of the conventional AVA

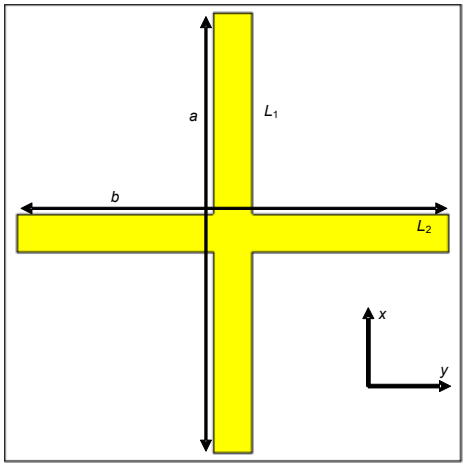

Fig. 3 Structure of the designed MLu

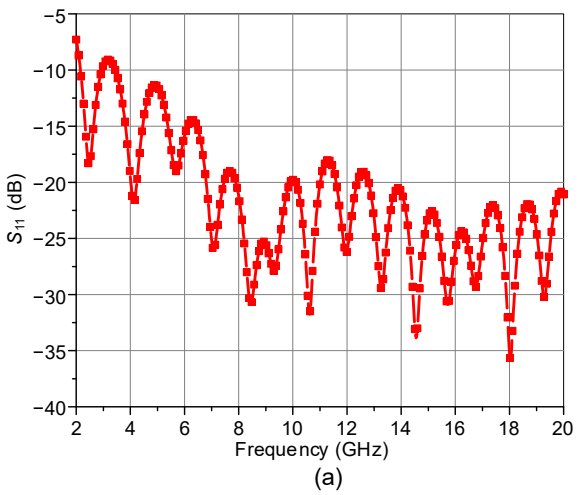

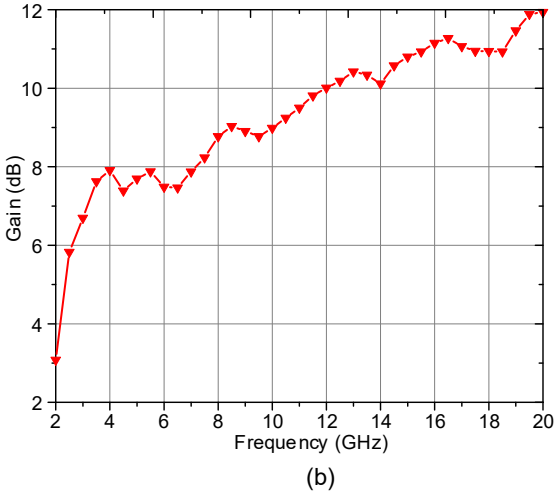

Fig. 2 Simulated S_{11} (a) and gain (b) of the conventional AVA

of the designed AVA. That is, the MLu will not affect the ultra-wideband characteristics of the AVA. The value of S_{21} is close to 0, indicating that the loss of the designed MLu is very small and negligible. It can be seen from Fig. 5 that the surface current is distributed mainly on the metal arm L_1 when the electromagnetic wave's polarization direction is along the x axis, while distributed mainly on the metal arm L_2 with the polarization direction along the y axis.

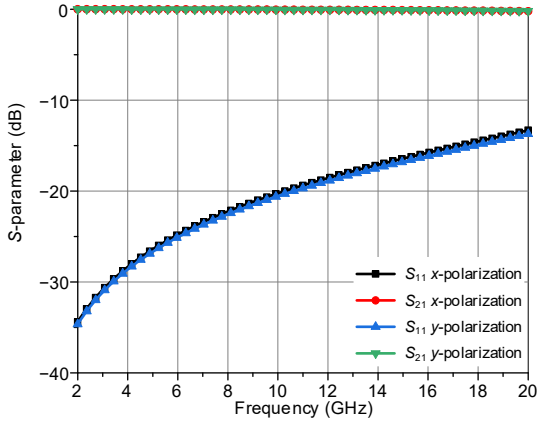

Fig. 4 Simulated *S*-parameters of MLu

We discuss the effect of a and b values on the effective permittivity and refractive index of the MLu excited by the two polarization modes electromagnetic waves. The simulation results are shown in Figs. 6 and 7. When the x-polarized electromagnetic wave excites the MLu, the value of a can significantly affect the effective permittivity and refractive index. The influence of b values on these two parameters is very small and can be ignored. When the y-polarized electromagnetic wave excites the MLu, changing the

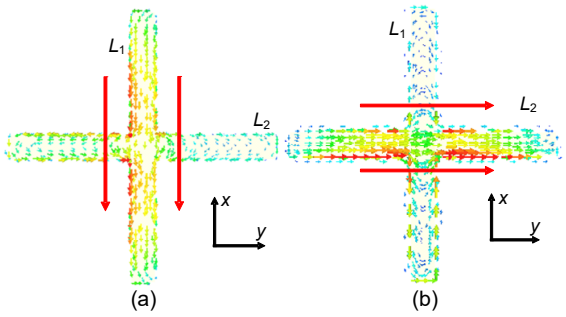

Fig. 5 Current distribution over the MLu at 14 GHz of *x*-polarization (a) and *y*-polarization (b)

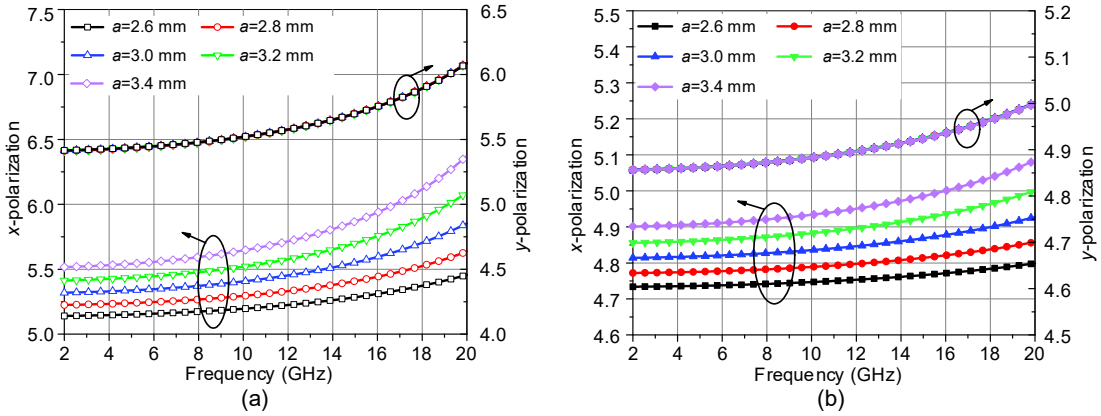

Fig. 6 Simulation results of the effective permittivity (a) and refractive index (b) of MLu with different *a* values

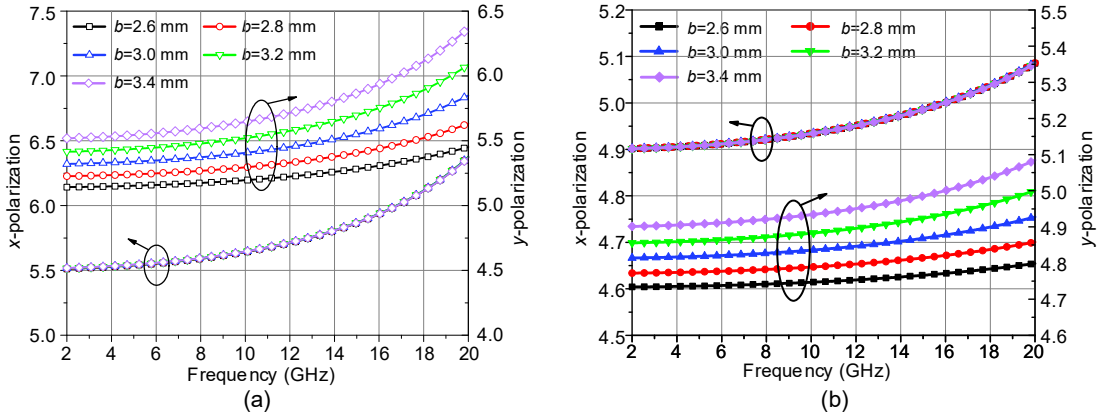

Fig. 7 Simulation results of the effective permittivity (a) and refractive index (b) of MLu with different *b* values

value of b will cause the effective permittivity and refractive index to change obviously. Therefore, the MLu can modulate the electromagnetic waves polarized in the x direction and y direction independently by adjusting a and b values. At the same time, with the excitation of electromagnetic waves in the two polarization modes, the effective permittivity of the MLu is above 5.0, which is greater than that of the substrate, so the designed MLu can be equivalent to a dielectric lens with high permittivity.

3.2 Antenna with metasurface lens design

As shown in Fig. 8, the designed MLu is arranged at the aperture of the AVA to form antenna Ant1. Fig. 9a shows the S_{11} simulation results that show no obvious changes of Ant1 compared with that of the AVA. The impedance bandwidth is 2–20 GHz, indicating that the loaded ML does not cause the deterioration of broadband performance. Fig. 9b shows the simulated gain of the AVA and Ant1. The gain of Ant1 has been significantly enhanced, especially in the 6–16 GHz frequency band. The maximum gain is increased by 3.5 dB. The downside is when the frequency is greater than 16.5 GHz, the gain of Ant1 begins to decrease and becomes even smaller than the gain of the AVA designed at 18 GHz. The radiation patterns of Ant1 at 17 and 18 GHz are shown in Fig. 10. The radiation patterns at the two frequencies have many grating lobes and the main lobe is split, resulting in the deterioration in directivity and gain.

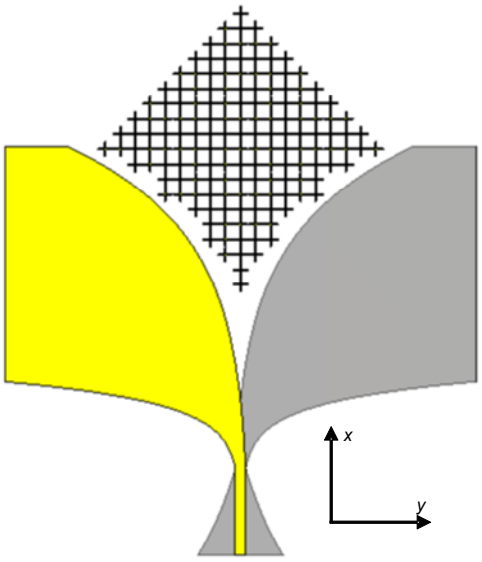

Fig. 8 Structure of Ant1

To further analyze the reasons for the deterioration of antenna gain, the electric field distributions of Ant1 at 14 and 18 GHz are compared. Fig. 11 shows the results of the electric field on the E-plane at two frequencies. After integrating the proposed high-permittivity ML on the antenna, the coupling between the radiating plates is enhanced. Under the guidance and modulation of the ML, the electric field is concentrated mainly at the antenna aperture, and the propagation path is expanded and flatters at 14 GHz. Fig. 11b shows that the electric field propagation path has also been expanded at 18 GHz, while the guidance and modulation of the electric field on both sides of the antenna aperture by the ML weaken as electromagnetic wave propagates forward. The electric field appears discontinuous at the arrows in Fig. 11b and propagates to the edge of the antenna aperture, which will cause the antenna radiation patterns to split and increase the grating lobes, thereby reducing the

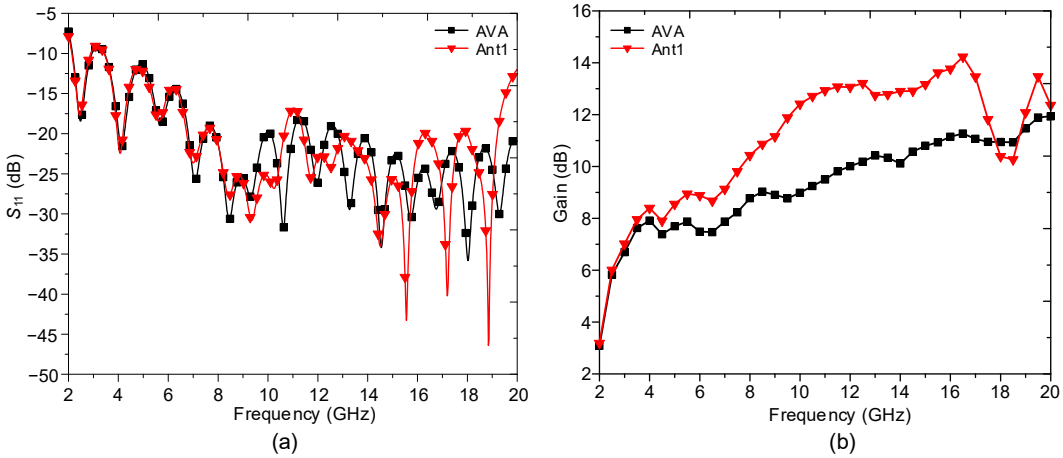

Fig. 9 Simulated S_{11} (a) and gain (b) of the AVA and Ant1

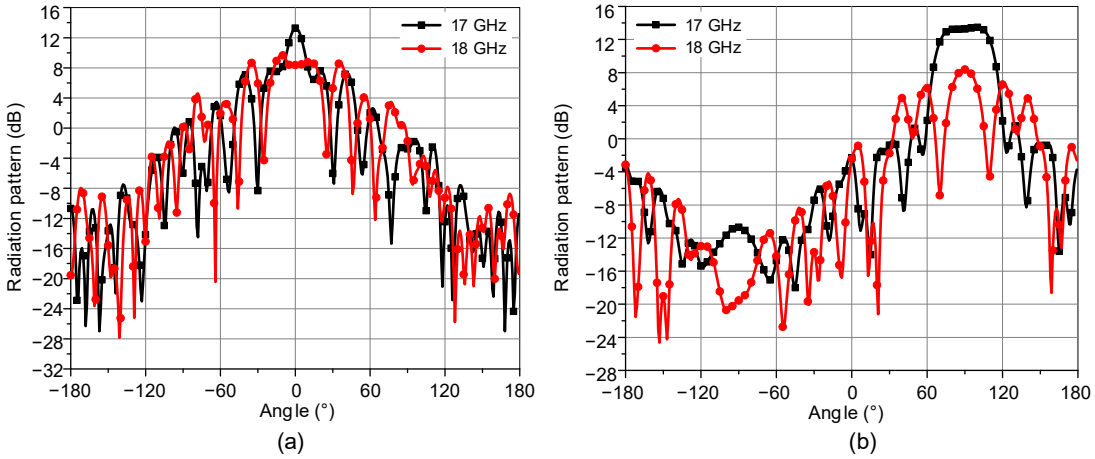

Fig. 10 Simulated E-plane (a) and H-plane (b) radiation patterns of Ant1 at 17 and 18 GHz

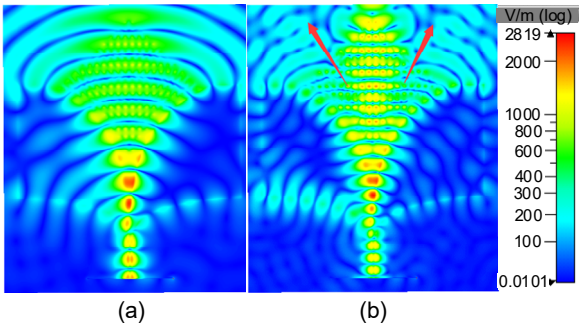

Fig. 11 Two-dimensional electric field distribution of Ant1 at 14 GHz (a) and 18 GHz (b)

antenna gain. Further analysis shows that the ML added by Ant1 is concentrated mainly at the center of the aperture, and that the MLu is not uniformly distributed and cannot fully guide or modulate the electric field. The phase of the electric field along the y axis at the antenna aperture is shown in Fig. 12. Compared with the AVA, the electric field phase at the Ant1 aperture has fluctuated and reversed many times, and the electric field distribution has been disturbed.

Fig. 13 shows the phase delay introduced by the MLu in the y-polarized electromagnetic wave. As shown in Fig. 14, the waves that pass through the edge produce more delay than the waves that pass through the center of the AVA. Therefore, to make the electric field distribution at the antenna aperture more uniform and reduce the phase distribution error, it is necessary to arrange more MLu in the center of the antenna aperture to provide more phase delay. The phase delays of the transmitted wave can be expressed by Eq. (3):

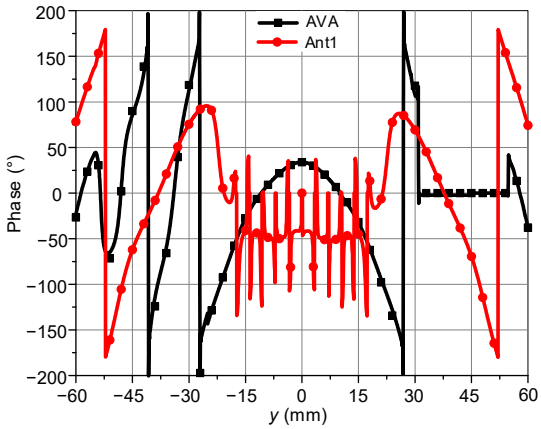

Fig. 12 Aperture electric field phase distribution of the AVA and Ant1 at 18 GHz

$$\begin{cases} \Phi_1 = \varphi_1 + \varphi_{11} + \varphi_{21} + \varphi_{31}, \\ \Phi_2 = \varphi_2 + \varphi_{12} + \varphi_{22} + \varphi_{32}, \\ \quad\vdots \\ \Phi_n = \varphi_n + \varphi_{1n} + \varphi_{2n}, \end{cases} \tag{3}$$

where φ_i (i=1, 2, …, n) represents the initial phase of the wave, and φ_{mi} (m=1, 2, 3) represents the phase delay of the MLu. When the phase delays of the transmitted wave satisfy Eq. (4), the transmitted wave has the same phase delay. The spherical wavefront at the antenna aperture is converted into a plane-like wavefront after passing through the ML, so the antenna can obtain a higher radiation gain.

$$\Phi_1 = \Phi_2 = \Phi_3 = \cdots = \Phi_n. \tag{4}$$

Based on the above principles, the ML as shown in Fig. 15 is designed and integrated on the aperture of the AVA to form Ant2. Numerical simulation

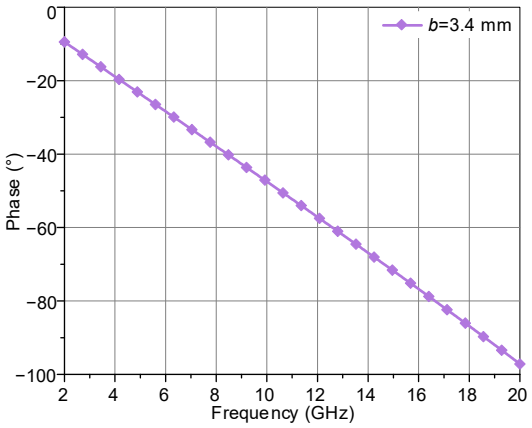

Fig. 13 Phase delay of the designed MLu

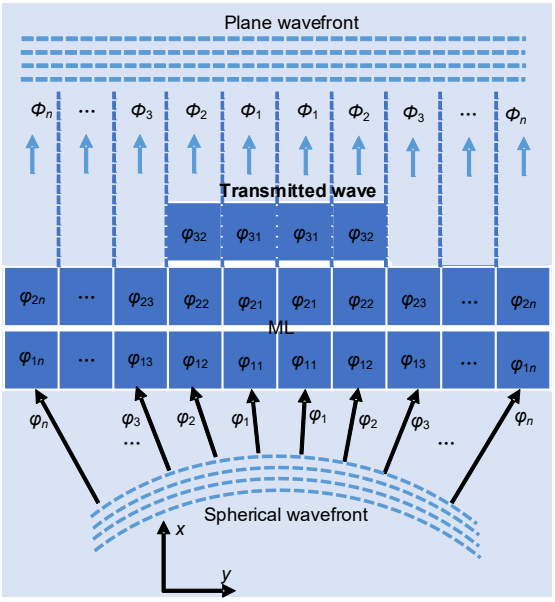

Fig. 14 Diagram of the ML which converts a spherical wavefront into a plane wavefront

analysis is performed on Ant2. Fig. 16a shows the S_{11} simulation results of the three antennas. The S_{11} result of Ant2 is basically the same as that of the AVA. There is only some disturbance in the high frequency range, and the impedance bandwidth is still 2–20 GHz. The gain results of the three antennas are shown in Fig. 16b. In the 2–16 GHz frequency band, the gains of Ant1 and Ant2 are significantly enhanced compared to the AVA. In addition, the designed Ant2 has a significant gain enhancement in the 16–18 GHz frequency band, with a maximum increase of 3 dB. The radiation patterns of the two antennas at 18 GHz are shown in Fig. 17. The sidelobe and the beam

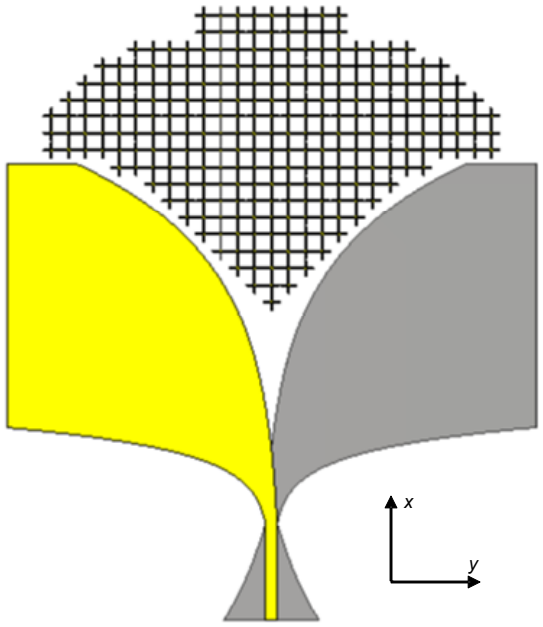

Fig. 15 Structure of Ant2

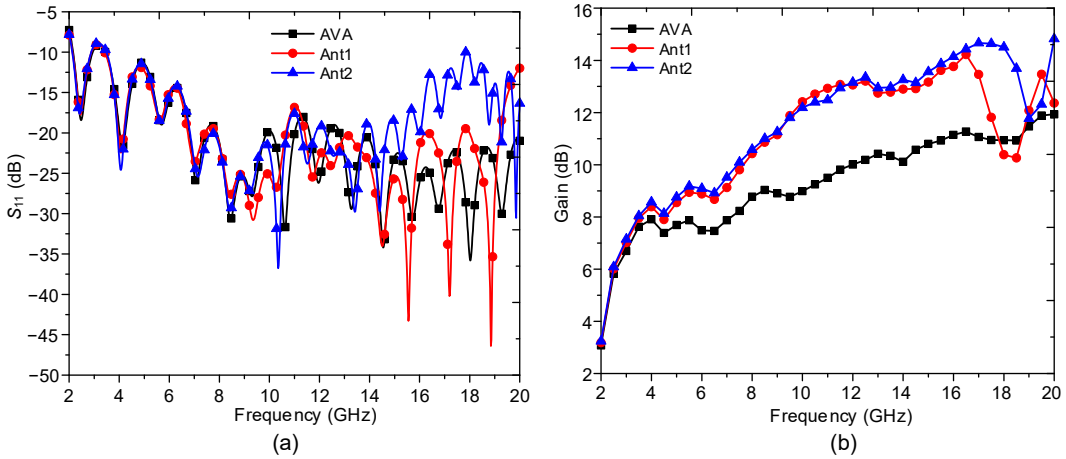

Fig. 16 Simulated S_{11} (a) and gain (b) of AVA, Ant1, and Ant2

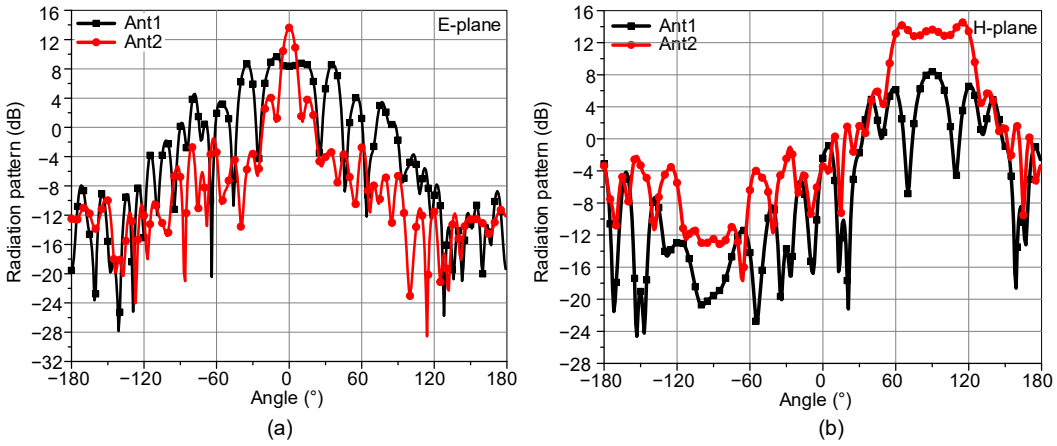

Fig. 17 Simulated E-plane (a) and H-plane (b) radiation patterns of Ant1 and Ant2 at 18 GHz

width of the Ant2 radiation pattern are reduced with the improvement of directivity.

Fig. 18 shows the electric field of Ant1 and Ant2 at 18 GHz. Compared with the former, the electric field of Ant2 is more uniform and planar. The electric field distribution at the edge of the antenna is also effectively suppressed, and the gain and directivity of the antenna can be enhanced. The phase of the electric field along the *y* axis at the antenna aperture is shown in Fig. 19. It is clear that the phase error on the Ant2 aperture is greatly decreased by integrating the ML. The smaller phase distribution error ensures the uniformity of the electric field distribution.

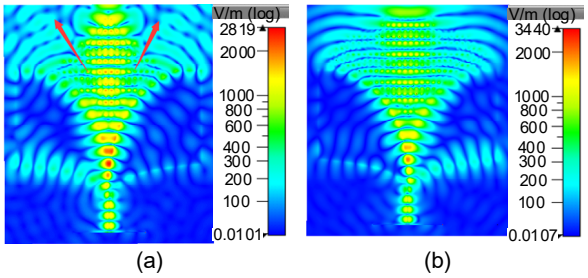

Fig. 18 Simulated 2D electric field on the E-plane of Ant1 (a) and Ant2 (b) at 18 GHz

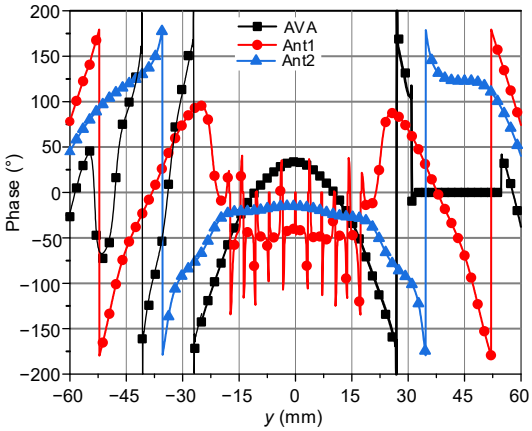

Fig. 19 Aperture electric field phase distribution of AVA, Ant1, and Ant2 at 18 GHz

4 Results and discussion

The AVA and the proposed Ant2 are fabricated, and photographs are shown in Fig. 20. Fig. 21 shows the two antennas measured in a microwave anechoic chamber. Because of the limitation of laboratory conditions, the radiation performance of two antennas between 2 and 18 GHz is measured and discussed. As shown in Fig. 22, the measured and simulated S_{11} results of Ant2 are well matched in the 2–18 GHz frequency band. The antenna substrate appears irregularly bent in fabrication, which disturbs the surface current distribution on the antenna. This is the main reason for the difference between the measured and simulated S_{11}.

Fig. 23 (see p.1664) shows the measured E-plane and H-plane radiation patterns of the AVA and designed Ant2 at the four frequencies of 6, 8, 10, and 12 GHz. The results of E-plane radiation patterns show that the gain and directivity of the designed Ant2 are improved, and that the sidelobe levels are reduced. Compared with the AVA, the beam width of the H-plane radiation patterns of the designed antenna is also reduced. Fig. 24 shows the measurement and simulation results of the gain of the two antennas. The gain of Ant2 in the 2–18 GHz frequency band is increased by 0.6–3.7 dB, which verifies that the designed ML can guide and modulate the electromagnetic wave at the antenna aperture

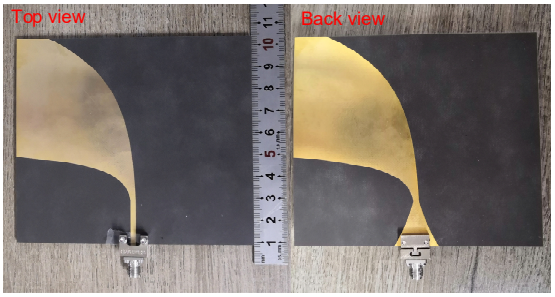

(a)

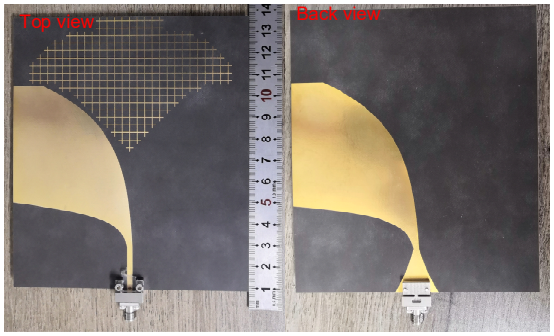

(b)

Fig. 20 Photographs of the AVA (a) and proposed Ant2 (b)

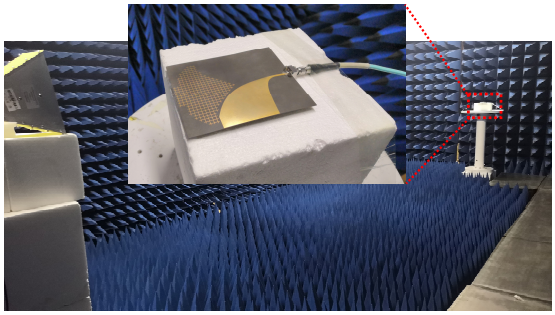

Fig. 21 Photograph of the antenna measured in a microwave anechoic chamber

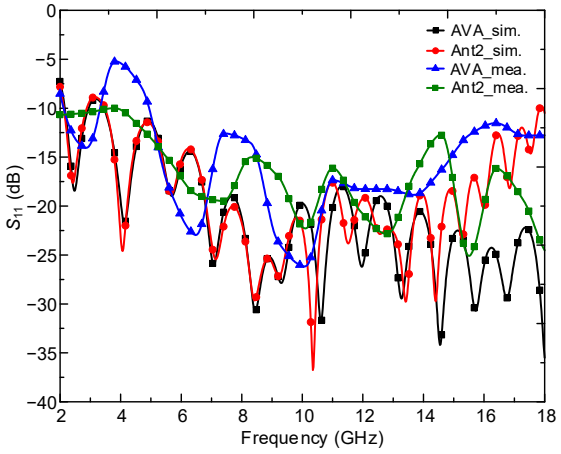

Fig. 22 Measured and simulated S_{11} results of the AVA and proposed Ant2

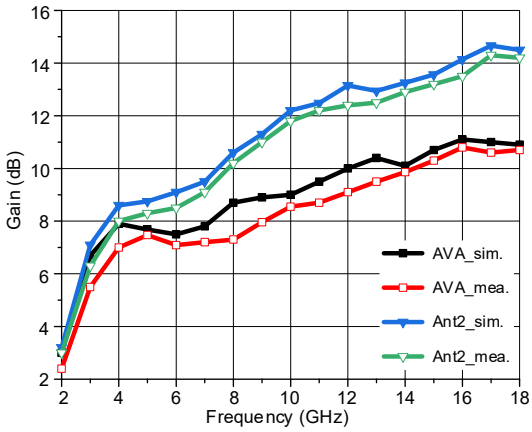

Fig. 24 Measured and simulated gain of the AVA and Ant2

favorably. The antenna fabrication error and other interference in the measurement are the reasons that the measurement and simulation results have some differences.

5 Conclusions

In this paper, we design a multi-octave bandwidth MLu that operates at 2–20 GHz. Good independent modulation ability of the MLu for two polarization modes electromagnetic waves is verified through the analysis of the surface current distribution, effective permittivity, and refractive index of the MLu. Two MLs are proposed and integrated into the aperture of the AVA, and the antennas Ant1 and Ant2 are designed. From the perspective of electric field amplitude and phase, the guidance and modulation effects of the ML on the electric field are analyzed, and the final ML loading method and antenna form are determined. The AVA and designed Ant2 are fabricated and measured, and the measurement results are in good agreement with the simulation ones. The measured impedance bandwidth of Ant2 basically covers the 2–18 GHz frequency band. Compared with the AVA, the Ant2 gain enhances by 0.6–3.7 dB in the 2–18 GHz frequency band and there is a significant enhancement in radiation performance.

Contributors

Shaopeng PAN designed the research. Lin QI and Pan CHEN measured the antennas. Yang FENG processed the data. Shaopeng PAN drafted the paper. Mingtuan LIN and Gaosheng LI revised and finalized the paper.

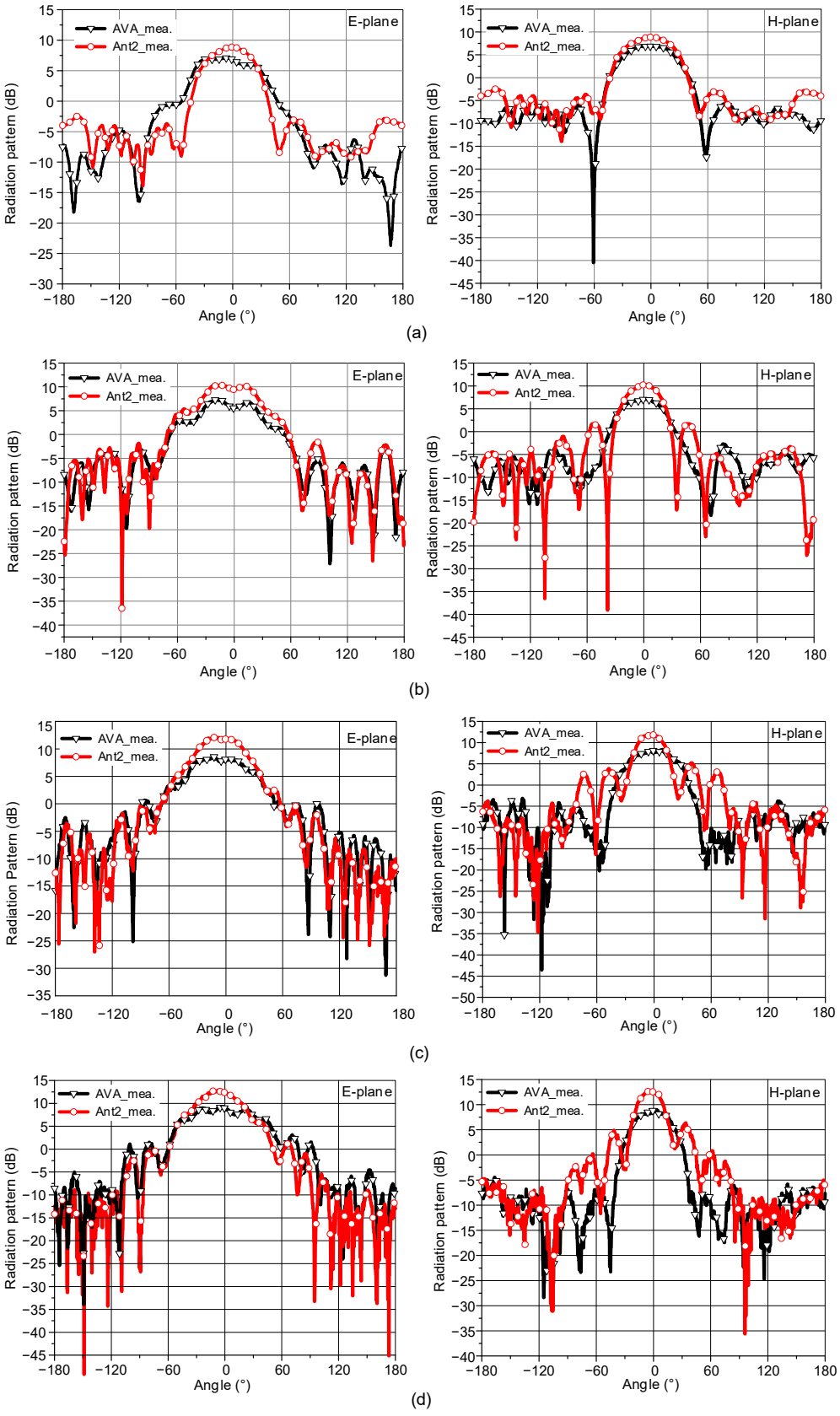

Fig. 23 Measured E-plane and H-plane radiation patterns of the AVA and proposed Ant2 at 6 GHz (a), 8 GHz (b), 10 GHz (c), and 12 GHz (d)

Compliance with ethics guidelines

Shaopeng PAN, Mingtuan LIN, Lin QI, Pan CHEN, Yang FENG, and Gaosheng LI declare that they have no conflict of interest.

References

Bourqui J, Okoniewski M, Fear EC, 2010. Balanced antipodal Vivaldi antenna with dielectric director for near-field microwave imaging. *IEEE Trans Antenn Propag*, 58(7): 2318-2326. https://doi.org/10.1109/TAP.2010.2048844

Chen L, Lei ZY, Yang R, et al., 2015. A broadband artificial material for gain enhancement of antipodal tapered slot antenna. *IEEE Trans Antenn Propag*, 63(1):395-400. https://doi.org/10.1109/TAP.2014.2365044

Gazit E, 1988. Improved design of the Vivaldi antenna. *IEE Proc H Microw Antenn Propag*, 135(2):89-92. https://doi.org/10.1049/ip-h-2.1988.0020

Gibson PJ, 1979. The Vivaldi aerial. Proc 9th European Microwave Conf, p.101-105. https://doi.org/10.1109/EUMA.1979.332681

Guo MJ, Qian RY, Zhang QS, et al., 2019. High-gain antipodal Vivaldi antenna with metamaterial covers. *IET Microw Antenn Propag*, 13(15):2654-2660. https://doi.org/10.1049/iet-map.2019.0449

Herzi R, Zairi H, Gharsallah A, 2015. Antipodal Vivaldi antenna array with high gain and reduced mutual coupling for UWB applications. 16th Int Conf on Sciences and Techniques of Automatic Control and Computer Engineering, p.789-792. https://doi.org/10.1109/STA.2015.7505195

Lewis L, Fassett M, Hunt J, 1974. A broadband stripline array element. Antennas and Propagation Society Int Symp, p.335-337. https://doi.org/10.1109/APS.1974.1147206

Liu W, Chen ZN, Qing XM, 2020. Dispersion-engineered wideband low-profile metasurface antennas. *Front Inform Technol Electron Eng*, 21(1):27-38. https://doi.org/10.1631/FITEE.1900473

Martín-Neira M, LeVine DM, Kerr Y, et al., 2014. Microwave interferometric radiometry in remote sensing: an invited historical review. *Radio Sci*, 49(6):415-449. https://doi.org/10.1002/2013RS005230

Moosazadeh M, Kharkovsky S, 2016. A compact high-gain and front-to-back ratio elliptically tapered antipodal Vivaldi antenna with trapezoid-shaped dielectric lens. *IEEE Antenn Wirel Propag Lett*, 15:552-555. https://doi.org/10.1109/LAWP.2015.2457919

Nassar IT, Weller TM, 2015. A novel method for improving antipodal Vivaldi antenna performance. *IEEE Trans Antenn Propag*, 63(7):3321-3324. https://doi.org/10.1109/TAP.2015.2429749

Pan SP, Shen WT, Feng Y, et al., 2021. Miniaturization and performance enhancement of Vivaldi antenna based on ultra-wideband metasurface lens. *AEU-Int J Electron Commun*, 134:153703. https://doi.org/10.1016/j.aeue.2021.153703

Sang L, Wu SR, Liu G, et al., 2020. High-gain UWB Vivaldi antenna loaded with reconfigurable 3-D phase adjusting unit lens. *IEEE Antenn Wirel Propag Lett*, 19(2):322-326. https://doi.org/10.1109/LAWP.2019.2961393

Sun M, Chen ZN, Qing XM, 2013. Gain enhancement of 60-GHz antipodal tapered slot antenna using zero-index metamaterial. *IEEE Trans Antenn Propag*, 61(4):1741-1746. https://doi.org/10.1109/TAP.2012.2237154

Yan JM, Hong H, Zhao H, et al., 2016. Through-wall multiple targets vital signs tracking based on VMD algorithm. *Sensors*, 16(8):1293. https://doi.org/10.1002/2013RS005230

Yesilyurt O, Turhan-Sayan G, 2020. Metasurface lens for ultra-wideband planar antenna. *IEEE Trans Antenn Propag*, 68(2):719-726. https://doi.org/10.1109/TAP.2019.2940462

Zhao HX, Li YF, Yin XX, 2017. Low cross-polarization Gaussian tapered post-wall slotline antenna for short pulse applications. *Int J Antenn Propag*, 2017:4852709. https://doi.org/10.1155/2017/4852709

Zhou B, Cui TJ, 2011. Directivity enhancement to Vivaldi antennas using compactly anisotropic zero-index metamaterials. *IEEE Antenn Wirel Propag Lett*, 10:326-329. https://doi.org/10.1109/LAWP.2011.2142170

Zhou B, Li H, Zou XY, et al., 2011a. Broadband and high-gain planar Vivaldi antennas based on inhomogeneous anisotropic zero-index metamaterials. *Prog Electromagn Res*, 120:235-247. https://doi.org/10.2528/PIER11072710

Zhou B, Yang Y, Li H, et al., 2011b. Beam-steering Vivaldi antenna based on partial Luneburg lens constructed with composite materials. *J Appl Phys*, 110(8):084908. https://doi.org/10.1063/1.3651376

Zhu SS, Liu HW, Wen P, et al., 2018. A miniaturized and high gain double-slot Vivaldi antenna using wideband index-near-zero metasurface. *IEEE Access*, 6:72015-72024. https://doi.org/10.1109/ACCESS.2018.2883097

Zhu SS, Liu HW, Wen P, 2019. A new method for achieving miniaturization and gain enhancement of Vivaldi antenna array based on anisotropic metasurface. *IEEE Trans Antenn Propag*, 67(3):1952-1956. https://doi.org/10.1109/TAP.2019.2891220

Zhuge XD, Yarovoy AG, 2011. A sparse aperture MIMO-SAR-based UWB imaging system for concealed weapon detection. *IEEE Trans Geosci Remote Sens*, 49(1): 509-518. https://doi.org/10.1109/TGRS.2010.2053038